PAPER

Check for updates

Secret agent in the secret service: Utilization of Sb(III)-based complexes' emission properties for the study of forgery and document authenticity†

Magdalena Rok, [iD] *[a] Aleksandra Krupińska, [iD][a] Marta Gordel-Wójcik, [iD][a]
Przemysław Szklarz, [iD][a] Przemysław Starynowicz, [iD][a] Piotr Durlak, [iD][a]
Rafał Janicki, [iD][a] Magdalena Malik, [iD][b] Ryszard Jakubas, [iD][a] Grażyna Bator [iD][a] and
Anna Piecha-Bisiorek [iD] *[a]

Document forgery, information leaks, and falsifying artworks, certificates, and diplomas have become increasingly sophisticated and challenging to detect. Therefore, designing materials whose response to external stimuli can be a perfect detector of crimes such as artifact forgery is crucial. Consequently, we decided to synthesize a functional material that exhibits strong broadband orange emission when exposed to UV light. This material is derived from organic–inorganic hybrids with the acronym **D4SB** (D4-dibutylammonium cation, Sb(III), B-ligand bromide). The **D4SB** crystal with stoichiometry (D4)$_3$[SbBr$_6$] undergoes one phase transformation at 166 K (heating cycle) in the solid state. A characteristic and unique property is that the phase transition (PT) changes the emission color to yellow in the low-temperature phase. Returning to the high-temperature phase reverses the light emission back to orange. According to the detailed spectroscopic characterization supported by the theoretical calculations, broadband light emission is associated with self-trapping excitons (STEs), resulting from a strong interaction between an electron and a phonon of the crystal lattice. Another advantage of this crystal is the easy mechanochemical synthesis in the solid, which speeds up the chemical reaction and requires no additional chemical solvents, making the synthesis environmentally friendly. We use this property to create the samples as thin films, which were initially used to confirm the authenticity of artifacts.

1. Introduction

In the modern world, technology is becoming increasingly advanced, making document forgery, information leaks, questioning of the authenticity of works of art, stealing intellectual property, counterfeiting money, and falsifying certificates and diplomas increasingly common and sophisticated. Document forgery is a crime that is difficult to detect, and various methods are used for this illegal activity: lithographic, steel engraving, xerographic, and typographic techniques, as well as computer processing and laser printing, to name a few. Such procedures threaten individuals and can take on an international character. The scope of its impact is much broader than it may seem, as it is inextricably linked to economic and political aspects, stability, and development. Therefore, new solutions are being sought, and new and existing technologies are being developed to protect against document forgery and to confirm the authenticity of artifacts. The most common are waterproof and holographic security, QR codes, RFID (Radio-Frequency IDentification) chips, blockchain technology, barcoding, or biometric methods. Among these techniques, an authenticity security strategy using photoluminescent (PL) materials (mainly quantum dots) is attracting widespread interest.[1–6] This is related to the fact that these materials have many advantages: a relatively simple technological process, low cost, and fast response to stimulus. In addition, PL materials do not change the appearance or structure of the document. These include compounds that emit visible light after ultraviolet (UV), near-infrared (NIR) excitation, or thermal activation. Molecular switches and metallic complexes are another group of photoluminescent (PL) materials being explored in applications for authenticity security.[7–11] Such a wide variety of

[a] *Faculty of Chemistry, University of Wroclaw, 14 F. Joliot – Curie, Wroclaw, 50-383, Poland. E-mail: magdalena.rok@uwr.edu.pl, anna.piecha-bisiorek@uwr.edu.pl*

[b] *Faculty of Chemistry, Wroclaw University of Science and Technology, Wybrzeże Wyspiańskiego 27, Wroclaw, 50-370, Poland*

This journal is © The Royal Society of Chemistry 2025

J. Mater. Chem. C, 2025, **13**, 17241–17250 | **17241**

materials shows that the problem is vivid and worth the effort expended.

Recently, results have been presented using PL organic–inorganic hybrids based on Sb(III) for anti-counterfeiting and encryption/decryption of sensitive information.[1] The new compound $(DPA)_3[SbCl_6]$ (DPA = dipropylammonium) showed strong green light emission with near-unity photoluminescence quantum yield. Therefore, encouraged by these results, a new compound was designed that is included in the haloantimonate(III) functional material group. The family of these compounds is defined by the general formula $R_aSb_bX_{3b+a}$ (where R – organic cations, and X = Cl, Br, I). The great advantage of these compounds is that by appropriately selecting the ratio of the organic to inorganic parts in the formula, it is possible to obtain compounds with various structures that generate many essential features from an application point of view.[12] In addition to the quantity aspect, the quality of the organic part is also a crucial factor. The size of the organic cation, symmetry, and the ability to form N–H···X-type hydrogen bonds can affect the structure of the anionic unit. In addition, the Sb(III) cation has a centered, stereochemically active lone electron pair ($5s^2$), which significantly affects the deformation of the anion. All these aspects should be taken into account when designing multidimensional spatial structures. A small organic cation with a spherical structure will favor two-dimensional (2D) or one-dimensional (1D) structures, while the utilization of sizeable organic cations markedly enhances the probability of attaining a 0D system. It is worth noting that the dimensionality of the structures is closely related to the stoichiometry of Sb(III) halogens. Many 2D and 1D hybrids based on Sb(III) exhibit ferroelectric properties with good spontaneous polarization characteristics or a small coercivity field.[13–18] They also find applications in light energy conversion, which is why they are being explored to replace toxic lead in photovoltaic cells.[19] In addition, they exhibit nonlinear optical[20–22] or semiconducting properties[23–25] and also have applications in catalytic research.[26–29] What is new recently is that compounds exhibit unique emission properties over a wide energy range, mainly within 1D and 0D groups.[1,30–47] Reducing the dimensionality to 1D or 0D might be achieved by using cations of relatively large size. These include both cations of aliphatic[30,35,37,39] and aromatic[31,33,36,38,48] amines. In the case of antimony halides, 0D structures are usually observed for the R_3SbX_6 stoichiometry, where single octahedra isolated by organic moieties construct the anionic sublattice. Sb(III) is coordinated by six halide ligands in this configuration, not shared by neighboring octahedra units. Consequently, the Sb–X bonds and the lone pair of $5s^2$ electrons are free to distort in the excited state, whose geometry differs significantly from the ground state. In such an architecture, guest–host systems are created in which light emitters are periodically embedded in the host matrix (organic cations) and completely separated without forming electronic bands.[1,37] The consequence is that these compounds exhibit luminescent properties such as high quantum efficiency, significant decay times, and light emission spanning the visible range.[1,39,49]

2. Results

2.1 Crystal structure determination

The crystals were obtained by simple synthesis in an aqueous medium acidified with a diluted water solution of HBr, in which dibutylamine (D4, $(C_4H_9)_2NH$) and Sb_2O_3 were dissolved in a molar ratio of 3 : 1, yielding crystals with a general formula $((C_4H_9)_2NH_2)_3[SbBr_6]$ (**D4SB**, Fig. 1a). The synthetic procedure, the data collection details, and the refinement of crystal structure (Table S1, ESI†) are described in the ESI.† The phase **I** (at 200 K) is trigonal, the space group being $R\bar{3}$.

The crystal is composed of two monomeric symmetry-independent $[SbBr_6]^{3-}$ anions, in which the Sb atoms are located in $\bar{3}$ rotoinversion centres. This implies that there are only two symmetry-independent Br sites: Br1 is connected to Sb1, and Br2 to Sb2. The Sb–Br bond lengths, which are unexceptional (*e.g.* ref. 36 and 50–52), are listed in Table S2 (ESI†). Both $[SbBr_6]^{3-}$ anions form slightly deformed octahedra, and the distortion applies only to the Br–Sb–Br angles. For 0D crystals, it is sporadic to find systems in which the $[SbBr_6]^{3-}$ units demonstrate a perfect regular octahedral geometry, with six identical Sb–X bond distances and X–Sb–X angles equal to 90°. Such a case has only been described for the $(DPA)_3[SbCl_6]$ system.[1] The reason for the octahedral distortion should be sought in the stereochemical effects of organic cations and the non-bonding $5s^2$ pair. In this structure, as can be seen in Fig. 2a, an organic veil isolates the inorganic octahedra from their neighboring units; the hexabromoantimonate anions are linked only to the dibutylammonium cations by N–H···Br hydrogen bonds (Fig. S2 and Table S4 in the ESI†).

The closest Sb···Sb distance of 9.9694(6) Å (phase **I**) or 9.770(5) Å (phase **II**) eliminates any significant electronic interactions between them. There is only one symmetry-independent dibutylammonium cation in the structure. The two outermost carbon atoms in one of its butyl parts, namely C6/C61 and C8/C81, are disordered (Fig. 2 and Table S3 in the ESI†). The cations with the C6–C8 fragment constitute 28.4(10)%, and those with the C61–C81 one – 71.6(10)% of all the cations. The 100 K phase (**II**) is triclinic, and the space group is $P\bar{1}$. There are 3 symmetry-independent Sb sites, one of which (Sb3) is located in a general position, whereas two others, Sb1 and Sb2, are in the inversion centers. All six symmetry-independent dibutylammonium cations are ordered (Fig. 2b). Table S2 (ESI†) lists the Sb–Br distances, and the view of the unit cell is shown in Fig. S3 (ESI†). The resulting three $[SbBr_6]^{3-}$ octahedra are distinct, each being deformed differently. More
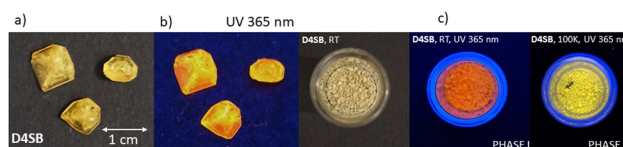

Fig. 1 Single crystals of the **D4SB** compound crystallized from an aqueous solution: (a) as observed under ambient light and (b) under UV light, showing intense orange luminescence. (c) **D4SB** powder in two temperatures, 300 (orange emission) and 100 K (yellow emission).
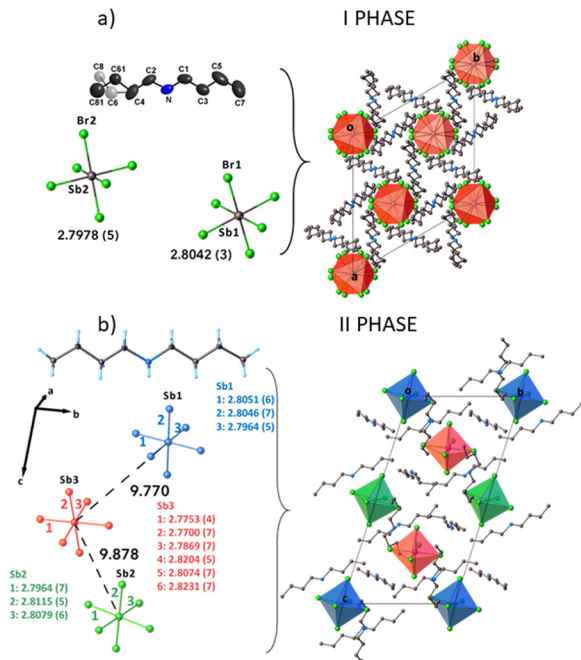
17242 | *J. Mater. Chem. C*, 2025, **13**, 17241–17250

This journal is © The Royal Society of Chemistry 2025

Fig. 2 (a) The dibutylammonium cation and the $[SbBr_6]^{3-}$ units in I phase are shown on the left. The hydrogen atoms have been omitted for clarity; the C6 and C8 atoms and the bonds involving them are transparent light grey. A view of the unit cell along the *c*-axis is presented on the right side. The Sb atoms are light grey, Br – green, N – blue, and C – grey. For clarity, the hydrogen atoms have been omitted. (b) The left side presents the cation and anions units in phase II. The right side depicts a view of the unit cell of phase II along the *a*-axis [OLEX2[53]].

analysis of the relationships between **I** and **II** phases is included in the ESI.†

2.2 Thermal analysis

Structural changes are associated with phase transformation (PT) in the solid state. In the case of the crystal under study, the temperature related to PT was estimated at 166 and 165 K in the heating and cooling cycles, respectively. Fig. S4a (ESI†) presents the thermal anomaly which was recorded with temperature ramps of 12 K min^{-1} for both heating and cooling cycles. The shape of the thermal anomaly and the small temperature hysteresis $\Delta T \sim 1$ K indicate the complex nature of the transformation. According to the structural data, the thermal effect is related to ordering the organic cations in phase **II** compared to phase **I**. The change in the anionic sublattice is also involved in PT. In phase **I**, we have two divergent $[SbBr_6]^{3-}$ octahedra; in phase **II**, we have three independent $[SbBr_6]^{3-}$ units. As described in the structural section, the differentiation is related to the deformation of the octahedra in both Sb–Br lengths and Br–Sb–Br angles. Fig. S4b (ESI†) shows the thermal stability of **D4SB**. The crystal melts at 350 K, and this low melting point is a characteristic of antimony complexes with reduced dimensionality.[38,39] Above 450 K, the crystal undergoes decomposition. The high stability of the crystal in contact with air has also been noticed. Exposure to air and moisture does not cause tarnishing.

2.3 Dielectric properties

The dielectric response of **D4SB** in a broad temperature region is illustrated in Fig. S5 in the ESI.† Structural changes alter only the slope of $\varepsilon'(T)$, and the observed small increment ($\Delta\varepsilon$) suggests that the phase transition at about 165 K is with small dielectric activity; more precisely, the structural changes do not affect the dipole moment orientation. Dielectric characteristic ($\varepsilon(T)$) in the vicinity of PT proves that the dipole–dipole interactions are relatively weak. Nevertheless, the shape of the dielectric anomaly close to T_c reflects the continuous freezing out of the dipoles in the low temperature phase.

2.4 UV-vis-NIR absorption spectra

UV-vis-NIR spectra of the monocrystal were obtained at different temperatures between 80 and 300 K. As discussed above, the observed phase transition is connected with ordering dibutylammonium cations at low temperatures. This is reflected in the spectral pattern of the $2\nu_{CH}$ overtone (1650–1850 nm) and $\delta_{CH_2} + \nu_{CH}$ combination bands (2100–400 nm). Furthermore, a substantial growth in the baseline of the spectra is observed when the temperature decreases from 180 K to 160 K (Fig. S6 in the ESI†). The spectra of thin films of the compound under study were also measured. The observed bands correspond to the following transitions: $^1A_{1g}$ ($^1S_0$) → $^3A_{1u}$ ($^3P_0$), $^1A_{1g}$ ($^1S_0$) → $^3T_{1u}$ ($^3P_1$), $^1A_{1g}$ ($^1S_0$) → $^3E_u + ^3T_{2u}$ ($^3P_2$) and $^1A_{1g}$ ($^1S_0$) → $^1T_{1u}$ ($^1P_1$). The $^1A_{1g}$ → $^3T_{1u}$ (see Fig. 5).[54]

The $^1A_{1g}$ → $^3A_{1u}$ transition is strictly forbidden; therefore, it is not observed in the absorption spectra. The $^1A_{1g}$ → $^3T_{1u}$ transition ($\sim 27\,200$ cm^{-1}) is partially allowed by the spin–orbit coupling, while the $^1A_{1g}$ → $^3E_u + ^3T_{2u}$ ($\sim 31\,200$ cm^{-1}) transition is lattice vibration assisted. Finally, the electric dipole allows the $^1A_{1g}$ → $^1T_{1u}$ transition observed at $\sim 34\,100$ cm^{-1}. Moreover, an additional band appears in the spectra below 190 K. The origin of this band is not clear, and it is probably part of the L → M charge transfer transition.[55] As seen in Fig. 3, the bands attributed to the $^1A_{1g}$ → $^3T_{1u}$ and $^1A_{1g}$ → $^1T_{1u}$ transitions predominate over the others and are split into two and three components, respectively. Moreover, the $^1A_{1g}$ → $^3T_{1u}$ band is strongly asymmetric compared to the other. The observed band splitting is caused by the Jahn–Teller effect. The energy of splitting of the $^1A_{1g}$ → $^3T_{1u}$ and $^1A_{1g}$ → $^1T_{1u}$ bands increases as the temperature rises and it is linearly dependent on the $\sqrt{T}$ as shown in Fig. S7 in the ESI.† The plot of the integral intensity of the $^1A_{1g}$ → $^3T_{1u}$ and $^1A_{1g}$ → $^1T_{1u}$ bands *versus* temperature is presented in Fig. S8 (ESI†). The intensity of both transitions remains constant between 300 K and 200 K. However, a jump is observed when the temperature is lowered below this range, which is probably caused by the phase transition. According to Toyozawa and Inoue,[56] the linear regression of the intensity ratio is defined as $R = \dfrac{I(^1A_{1g} \rightarrow ^1T_{1u})}{I(^1A_{1g} \rightarrow ^3T_{1u})}$ and the $\sqrt{kT}$ factor gives the coupling constant c, which in our case was found to be equal to 278 ± 4 cm$^{-1/2}$. This supports the conclusion that the Jahn–Teller effect is the
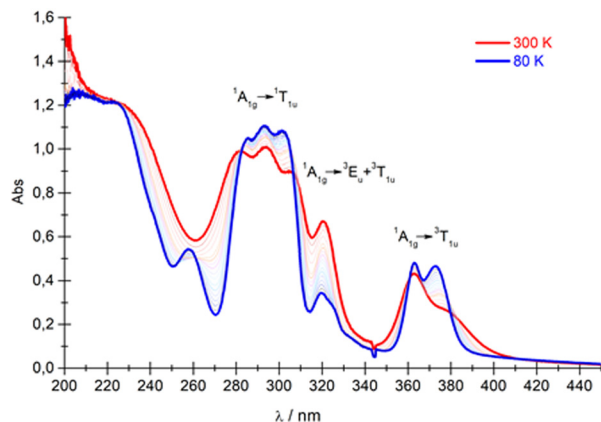
This journal is © The Royal Society of Chemistry 2025

J. Mater. Chem. C, 2025, **13**, 17241–17250 | **17243**

Fig. 3 UV-vis absorption spectra of **D4SB** under study in thin films at different temperatures.

Fig. 4 Temperature dependence of the excitation spectra of **D4SB** obtained for the maximum emission at 700 nm (a) and (b) and 600 nm (c) and (d).

underlying mechanism of excited state splitting, as the T_{2g} active modes of the lattice vibrations couple with the excited T_{2u} electronic states, removing their degeneracy.

Finally, the energy band gap was determined for both monocrystalline samples as well as for the thin film. The band gap value was found to be 2.95 eV and 3.14 eV for the crystalline and thin film samples, respectively. The obtained compound can be classified as a conductor.

2.5 Excitation and emission characteristics of D4SB

The compound **D4SB** crystallizes as dark yellow crystals, which, when exposed to UV light (365 nm), emit orange light that can be observed with the naked eye (Fig. 1b). When the crystals are immersed in liquid nitrogen, a change of the emission color to yellow is observed (Fig. 1c). Upon reheating, the emission color returns to orange. Photoluminescence measurements over a wide temperature range were performed to investigate the nature and origin of these emissions. Commission Internationale de l'Éclairage (CIE) chromaticity coordinates are calculated to be (0.60, 0.39) and (0.56, 0.44) for 300 (phase **I**) and 100 K (phase **II**), respectively (Fig. S11a in the ESI†). First, the excitation (PLE) spectra of the sample were collected as a variable as a function of temperature for two emissions at 600 and 700 nm. In the case of phase **I** (Fig. 4a and b), the excitation spectrum is illustrated as a single broadband whose intensity increases as the temperature decreases. This increase in intensity is observed up to a temperature of 170 K. However, near PT, a noticeable drop in intensity occurs below this temperature. For excitation spectra measured at 600 nm, the intensity of the band similarly increases with decreasing temperature (Fig. 4c and d).

However, this spectrum exhibits distinct characteristics compared to the previous one. The first difference is related to the abrupt change in band intensity near the phase transition (at 170 and 150 K). Additionally, as the temperature decreases further from 150 to 15 K, the band maximum shifts toward higher energies within phase **II**. Fig. S9 (ESI†) presents a 3D PL excitation and emission correlation map for two temperatures, 300 K (phase **I**) and 50 K (phase **II**). The maps show
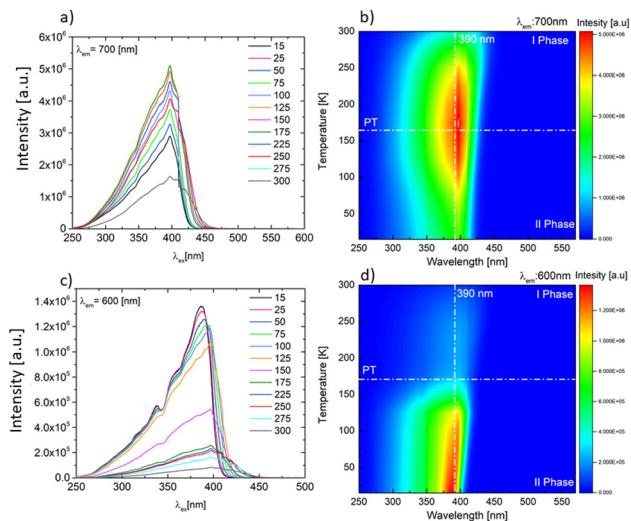
one dominating emission at 700 and 600 nm for phases **I** and **II**, respectively. Following the spectra presented in Fig. 4b and d, the excitation wavelength of 390 nm, for which the emission spectra are quite intense in phase **I** and phase **II**, was chosen to observe the photoluminescence properties.

The photoluminescence (PL) phenomenon arises from the radiative recombination of electron–hole pairs (excitons). The interaction force between the electron and hole is defined by the binding energy (E_b) of the exciton (Fig. 5d). If this energy is relatively low, bright emissions can be observed only at low temperatures. Increasing the temperature transforms the exciton into free charge carriers, decreasing the PL intensity.[25,57] However, lowering the dimensionality of the structure to 0D improves the emission performance of the sample. There are many reports of Sb(III)-based hybrid materials where broadband emission with high quantum efficiencies and generally longer lifetimes ($\sim\mu s$) is observed at RT.[1,42–44,58] This effect results from exciton becoming localized due to strong coupling with the crystal lattice. As for semiconductors with soft crystal lattices, strong exciton–phonon coupling (EPC) can cause a transient elastic lattice distortion surrounding excited electron/hole pairs after excitation, leading to a self-trapped state (STE). The exciton will lose some energy (self-trapping energy, E_{st}) due to the formation of STEs. Energy E_{st} corresponds to the energy difference between the free exciton state (FE) and STE. Additionally, the energy of the ground state (GS) will rise due to lattice deformation (E_d). Therefore, the energy associated with the emission can be described by the following equation: $E_{PL} = E_g - E_b - E_{ST} - E_d$, resulting in the significant Stokes shift (>50 nm) in broadband STE emission. A detailed analysis of the PL emission spectra of **D4SB** was conducted at different temperatures, in the range between 13 and 300 K (Fig. 5a–c). The temperature range covers the areas of the two phases (**I** and **II**) in the solid state. At 300 K, the observed PL emission spectrum is a broad band with a maximum wavelength of
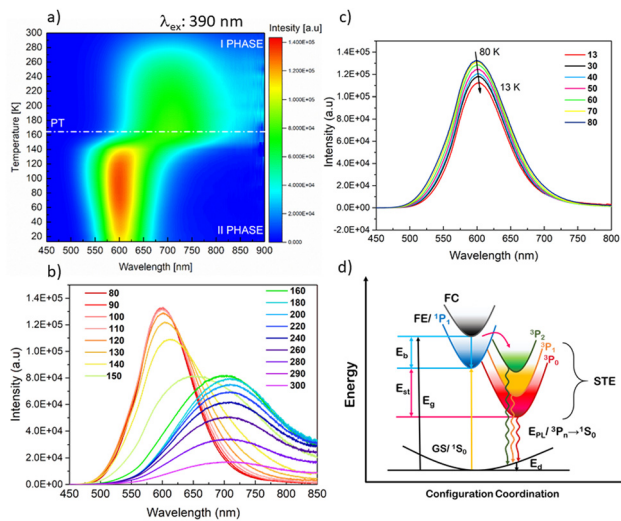
17244 | J. Mater. Chem. C, 2025, **13**, 17241–17250

This journal is © The Royal Society of Chemistry 2025

Fig. 5 (a) Temperature dependence of the emission spectra at 390-nm excitation. The correlation is shown in the form of a two-dimensional map (a) as well as in two temperature ranges, 80–300 K (b) and 13–80 K (c). (d) Schematic diagram of the energy level structure of STE (GS, ground state; FE, free exciton state; FC, free carrier state; STE, self-trapping state; E_g, bandgap; E_b, exciton binding energy; E_{st}, self-trapping energy; E_d, lattice deformation energy; E_{PL}, emission energy).

700 nm. The band has the ideal shape of a Gaussian function with a full-width at half-maximum (FWHM), Γ_{FWHM}, of 206 nm and a Stokes shift of 314 nm (Fig. S11a, ESI†). As the temperature decreases, the intensity of the band increases (Fig. 4b). In the vicinity of the phase transition, the position of the band maximum shifts toward high energies when temperature decreases. Due to the asymmetric nature of the bands for two temperatures (140 and 150 K) near PT, two Gaussian functions were used for the fitting (Fig. S11b, ESI†). For temperatures below 140 K, fitting with one component was sufficient (Fig. S11c, ESI†). For temperatures spanning the phase **II** region, a band maximum (80 K) is observed for a wavelength of 600 nm with Γ_{FWHM} 106 nm and a Stokes shift of 210 nm (Fig. 4b). Narrowing the PL spectra at low temperatures is associated with reduced thermally populated vibrational states.[59] For temperatures below 80 K, a decrease in band intensities is observed on cooling (Fig. 4c) due to antithermal quenching behavior.[1,60] Sometimes, broadband light emission comes from deep traps on surface defects and depends heavily on particle size.[61,62] PL measurements were performed on monocrystalline and polycrystalline samples (a hand-grated crystal in a mortar) to confirm whether the broad emission is intrinsic or originated from an extrinsic surface defect. Fig. S10b (ESI†) shows that µc-sized powder has the same emission spectrum as bulk crystals. The conclusion is that the observed emission results from material properties and not structural defects.

In our study, the emission lifetimes were monitored for both phases across different temperature ranges. Precisely, the lifetime of the emission band at 600 nm was measured between 15 K and 150 K, while the 700 nm emission was analyzed in the 150–300 K range. In both cases, the observed lifetimes were on

the order of a few microseconds. The most extended lifetime was recorded for the 600 nm emission at 15 K, reaching 2.77 µs. In contrast, the shortest lifetime, 1.24 µs, was observed for the 700 nm emission at 300 K. Notably, at 150 K, a broad emission band appears (see Fig. 5b), potentially indicating the emission from two distinct phases. However, the emission lifetimes monitored at this temperature for the 600 nm and 700 nm bands show no significant differences, measuring 2.12 µs and 2.48 µs, respectively (see Fig. S11 and Table S5, ESI†).

The mechanism of emission in the **D4SB** crystal can be explained as follows (Fig. 5d): for the Sb(III) cation, the ground state is described by the energy level $^1S_0$. The excited state, originating from the 5s5p orbital, gives rise to four levels, namely, $^3P_0$, $^3P_1$, $^3P_2$, and $^1P_1$. The transition from the base level $^1S_0$ to $^1P_1$ is allowed, while the spin–orbit coupling partially allows the transition from $^1S_0$ to $^3P_1$. In both cases, phase **I** and **II**, under the excitation of 390 nm electrons, it is excited from $^1S_0$ to single state $^1P_1$, and then rapidly relaxed into triple state ^3P_n ($n = 0, 1, 2$) levels through intersystem crossing (ISC) to form self-trapped excitons. Eventually, it will return from the STE state to the GS, emitting broadband light emission with large Stokes shifts. The strong electron–phonon interaction mathematically can be tentatively described by the Huang–Rhys relationship (see *e.g.* ref. 4 in the ESI†), where the factor S is introduced.[63] The value of this parameter is correlated with the probability of STE formation. Fig. 6a presents the temperature dependence of the half-width in two phases (**I** and **II**) and the function fitted to the points according to eqn (4) in ESI.† The determined S values are 86.1 and 14.9 for phase **II** and **I**, respectively. In the case of phase **II**, the S value is relatively large for halogen hybrid systems. From the literature data, the value ranges between 10 and 40 units.[31,32,35–37] The value of 86.1 suggests a very high electron–phonon coupling, which may account for the antithermal quenching behavior from 80 to 15 K (Fig. 5c). Due to this behavior for the low
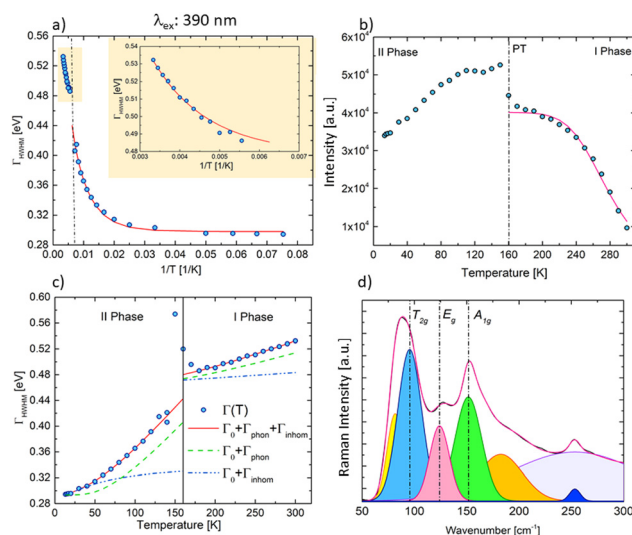

Fig. 6 Temperature-dependent FWHM of the PL spectra (a) and (c), and integrated PL intensity (b). (d) Raman spectrum of **D4SB** under 1064 nm excitation.

This journal is © The Royal Society of Chemistry 2025

J. Mater. Chem. C, 2025, **13**, 17241–17250 | **17245**

temperature region (phase **II**), the integrated PL intensity of **D4SB** crystals data were fitted by eqn (S5) (ESI†) only for temperatures from phase **I** (Fig. 6b). Based on the data, the activation energy (E_b) can be obtained using the Arrhenius relationship. This energy is defined as the binding energy between electrons and holes during exciton formation, and for **D4SB** equals 274.4 meV, which is higher than that of three-dimensional metal halides[66,67] as well as the other organic–inorganic hybrids of Sb(III)[35,44] as a result of the radiative recombination of localized excitons.

Raman spectroscopy was performed to detect the lattice distortion that induces STE. Fig. 6d presents the Raman spectra measured in the wavenumber region corresponding to $[SbBr_6]^{3-}$ vibration modes. In particular, it was found that the three intense bands at 87, 123, and 153 cm^{-1} perfectly satisfy the following general relationship for octahedra, $\nu_{A_{1g}}^2 \approx \nu_{E_g}^2 + \frac{3}{2}\nu_{T_{2g}}^2$, where A_{1g}, T_{2g}, and E_g are the symmetric stretching, bending, and asymmetric stretching modes in octahedrons, respectively, which further verified strong electron–phonon interaction in the $[SbBr_6]^{3-}$ octahedron.[68,69] A very intense band in the Raman spectrum at 87 cm^{-1} may include a contribution from elastic scattering (Rayleigh scattering). The Raman spectrum measured from 50 to 4000 cm^{-1} is included in Fig. S12 (ESI†).

As a result, the evolution of $\Gamma_{FWHM}(T)$ derived from the broad emission can be described by the Fröhlich[70] longitudinal optical (LO) phonon broadening model [*e.g.* ref. 6 in the ESI†]. The constants Γ_{phonon} and Γ_{inhomo} give the relative contributions of EPC and inhomogeneous broadening induced by trapped states, respectively. As shown in Fig. 6c the best fitting in phase **II** gives 297.5, 382.12, 18.89, 32.6, and 3.91 meV for, Γ_0, Γ_{phonon}, E_{LO}, Γ_{inhomo}, and E_{inhomo}, respectively. For phase **I** the parameters are as follows: $\Gamma_0 = 441.6$ meV, $\Gamma_{phonon} = 97.6$ meV, $E_{LO} = 18.87$ meV, $\Gamma_{inhomo} = 11.14$ meV, and $E_{inhomo} = 4.32$ meV. In both phases, the E_{LO} is well consistent with the intense stretching Sb–Br band obtained by Raman spectroscopy ($\sim$153 cm^{-1}). It is worth emphasizing that in the case of phase **II**, the energy associated with EPCs is much higher than that obtained in phase **I**. It also exceeds those recorded in similar systems.[1,37,64,71,72] The results presented here confirm the significant influence of electron–phonon coupling (EPC) in the soft 0D crystal lattice on the formation of STE states and, consequently, the observation of broadband light emission.[65]

The crystal cooled to phase **II** changes the emission color to yellow when excited with 365 nm light. During the heating cycle, the color returns to red-orange. The effect is related to the fact that the surroundings of the $[SbBr_6]^{3-}$ octahedra change due to the phase transition. One can make conclusions by analyzing the specific interactions presented in Table S4 in the ESI.† Due to the phase transition from phase **II** to **I**, "loosening" of the structure occurs, and the freedom of motion of $[SbBr_6]^{3-}$ units considerably increases. A similar effect was observed for α-[DHEP]SbCl$_5$ and β-[DHEP]SbCl$_5$–2H$_2$O (DHEP-1,4-di(2-hydroxyethyl)piperazine).[47] The loosening of the environment of $[SbBr_6]^{3-}$ units enhances the excited-state structural deformability and distortion level, which reduces the

energy level of the STE state and causes an evident shift of the emission wavelength toward lower energies.

Flattening of the wave in the band structure, *i.e.*, the presence of bands with low dispersion (flat bands), is associated with a low group velocity of electrons (Fig. S13, ESI†). This may suggest that the electrons are strongly localized in space, which typically results from effects such as strong electron localization, correlation effects, crystal lattice geometry, and topology. The crystal structure can promote the formation of flat bands, for instance, in materials with specific symmetries or frustrated lattices. Concerning the connection to low electron density, flat bands do not necessarily indicate low electron density. Low electron density (*i.e.*, the number of electrons per unit volume) is more closely related to the chemical composition and the number of free electrons in the crystal. However, in materials with low electron density, effects related to electron localization are often observed, which can lead to the emergence of flat bands. Conversely, high electron density tends to favor more "diffuse" bands resulting from greater electron delocalization.

In summary, band flattening may, but does not necessarily, indicate low electron density. It is more likely associated with electron localization, the geometry of the crystal structure, and correlation effects. The chemical composition and the characteristics of the crystal lattice in the studied crystals may suggest low electron density within the unit cell.

2.6 Synthesis of D4SB crystals by mechanochemical methods

The studied crystals were obtained classically through so-called wet synthesis, where dibutylammonium bromide (D4-HBr) was combined in an aqueous solution with SbBr$_3$ in the appropriate stoichiometry (3 : 1 for D4 : Sb). Difficulties encountered during this synthesis included the crystallization of the D4-HBr salt itself as a thin layer on the surface of the solution (Fig. S1, ESI†). The formation of a thin layer of one of the substrates on the surface of the solution negatively affects the total crystallization of **D4SB**, either by increasing the evaporation time of the solution or by using different proportions of solvents (water, methanol). Therefore, attempts were undertaken to synthesize compounds by mechanochemical methods, in which mechanical energy was used to initiate or accelerate a chemical reaction. A considerable advantage of this method is that there is no requirement for solvents or high temperatures, making it more environmentally friendly. It increases the response velocity, reduces the product's waiting time, and does not require specialized equipment; only a mortar or ball mill is needed for the basics. First, two salts, D4·HBr (0.76 g) and SbBr$_3$ (0.43 g), were ground in a mortar. Surprisingly, the hybrid synthesis occurred automatically at the interface between the two salts, as seen in Fig. 7a. Next, two dry salts were ground together for 3–5 min (Fig. 7b). In the second approach, the LAG (liquid assistant grinding) method was used, in which 2–3 drops of methanol were added to the identical aliquots. This yielded a much easier paste to grind (Fig. 7c).

To determine whether the resulting compound has the same structure as the **D4SB** monocrystal, powder X-ray analysis
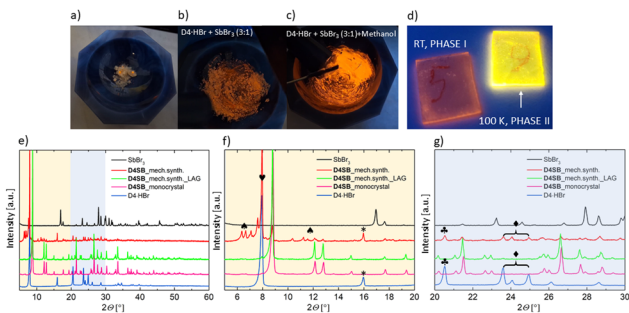
17246 | *J. Mater. Chem. C*, 2025, **13**, 17241–17250

This journal is © The Royal Society of Chemistry 2025

Fig. 7 (a) Image of substrates, (b) image of products after 5 min of grinding of D4·HBr and SbBr$_3$ (3:1), and (c) image of products after 5 min of LAG grinding of D4·HBr and SbBr$_3$ (3:1) with few drops of methanol. (d) Thin layer of **D4SB** under UV (365 nm) at two temperatures: RT (orange) and 100 K (yellow). (e), (f) and (g) X-ray powder diffraction was performed on substrates and products in various forms (blue D4·HBr, pink **D4SB**_monocrystal, green **D4SB**_LAG, red **D4SB**_mech.synthesis, black SbBr$_3$).

(PXRD) was performed. PXRD was performed for both substrates (D4·HBr and SbBr$_3$) and three product samples: grated monocrystalline **D4SB**, powders obtained by dry mechanochemical synthesis, and LAG. Fig. 7e and f show a powder diffractogram with the differences marked. The positions of the reflections recorded for the powder, obtained by the LAG method, coincide with those measured for the grated monocrystal. Some discrepancies appear for dry mechanochemical samples. Reflections 2θ in the range 6.3–7.6 and 10.3–11.6 (marked by ♠) indicate that the sample is not structurally homogeneous. On the other hand, reflections at positions 7.9 (♥), 16 (*), and 20.56 (♣), and in the range from 23.6 to 25 (♦) demonstrate that one substrate (pure D4·HBr) did not react 100%. The conclusion that can be drawn from this part of the study is that the **D4SB** crystals can be obtained quite easily by mechanochemical synthesis, and adding a few drops of methanol (LAG method) increases the efficiency of this method.

2.7 Fabrication of thin films of D4SB

The next step involved the sample preparation as a thin film. For this purpose, solutions of 30% concentration were prepared and spin-coated onto an early prepared substrate (more details can be found in the ESI†). Generally, the time of the solution depositing was fixed (35 s), and the following fresh, thin layers were annealed at 323 K for 15 min. In order to ultimately develop layers, the samples were left at RT for 4–6 h. Two methods, static and dynamic, were used to estimate which gives the thin layer the best quality. In the dynamic method, the solution is deposited onto a rotating substrate instead of the static method, where the solution is first spotted onto the substrate, and then the entire system is put into rotary motion. The frequency of the rotation was 3000 rpm in both cases. Fig. 8a includes thin films in two sources, light and UV (364 nm).

Additionally, images obtained with an electron microscope (SEM) were presented to screen the layers' transparency. With the rotation of 3000 rpm, in the case of the dynamic method,
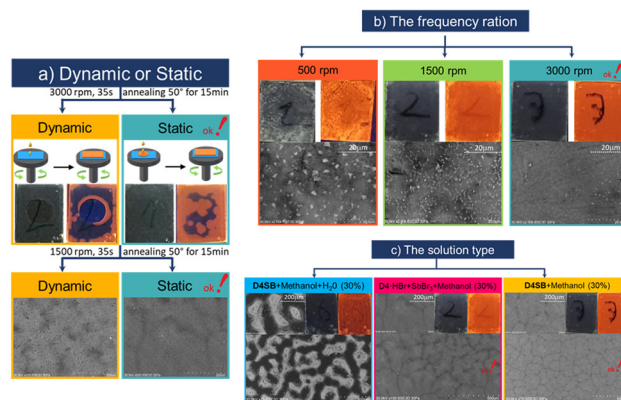

Fig. 8 (a) Comparison of two dynamic and static methods during thin film fabrication. (b) Imaging of the fabricated thin films using the static method depending on the rotation frequency: 500, 1500, and 3000 rpm. (c) Generation of thin films by dissolving **D4SB** crystals (right), D4·HBr, and SbBr$_3$ substrates in methanol (center). The left part shows the layers that were obtained in solvent with the addition of water.

depositing the solution on a moving substrate causes the layer to be uneven throughout the volume. In this case, we noticed that the solution at the spotting point is blown out outward. In addition, images obtained from the SEM analysis indicate that the surface of the thin film may be rougher than that obtained statically.

The rotation frequency also affects the quality of the layer. Fig. 8b shows the collected results for three selected rpm frequencies: 500, 1500, and 3000 rpm. In this case, the quality of thin films strongly depends on the rotational speed. For frequencies lower than 3000 rpm, **D4SB** crystallites are formed on the surface of the film, thus increasing an undesirable parameter like sample roughness.

Our next step is to determine the effect of the solution preparation on the quality of the film produced. The results we gained in solid-state synthesis are essential for this stage. Fig. 8c shows the results from three different ways of producing a thin film. The first way is to dissolve **D4SB** crystals in methanol, previously crystallized in the classical way (wet synthesis). The second way is to dissolve D4·HBr and SbBr$_3$ substrates (3:1) in methanol before producing the thin film, and both solutions are 30%. The third type of solution included the aqueous component. Water was added to the **D4SB** solution (30%) until turbidity appeared. Syringe filters filtered all solutions before depositing. No significant differences exist in the film quality produced by dissolving the **D4SB** crystals in methanol or by dissolving the substrates (with the appropriate stoichiometric ratio). In contrast, adding water deteriorates the quality of the resulting layer, which is visible to the naked eye. The SEM image shows spots of nanocrystal aggregation, meaning the layer is inhomogeneous. In summary, the best method that produces thin films of good quality in the case of **D4SB** is the static method. The rotation frequency should be 3000 rpm, an excellent solvent is methanol, and it does not matter whether we use the product or the initial substrates for synthesis.
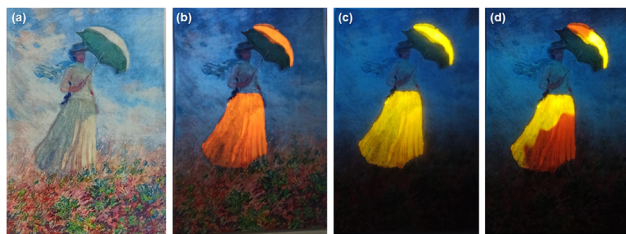
This journal is © The Royal Society of Chemistry 2025

J. Mater. Chem. C, 2025, **13**, 17241–17250 | **17247**

Fig. 9 (a) Reproduction of Claude Monet's painting (Woman with a Parasol, facing right, 1886) with sections (skirt and umbrella) painted with **D4SB** in methanol. (b) Image at RT in UV (366 nm), and (c) image immersed in liquid nitrogen after 365 nm excitation (UV lamp). (d) Emission color change due to heating from liquid nitrogen to RT. The color change is related to the thermal and emission properties of **D4SB**.

Unique multiple emission switching of **D4SB** allows this compound to be used in confidential documents and anti-counterfeiting applications. High thermal stability, low hygroscopicity, easy synthesis, and the compound application method on parchment encouraged us to test the compound in this aspect. Organic–inorganic complexes based on Sb(III) halides rarely dissolve in organic solvents without the addition of suitable mineral acids (HCl, HBr, or HI). In this case, the product (**D4SB**) and the substrates (D4·HBr and SbBr$_3$) are perfectly soluble in solvents like methanol or ethanol. Below (Fig. 9a) is a reproduction of a Claude Monet painting (Woman with a Parasol, facing right, 1886), printed on laboratory paper using a laser printer. Selected parts (skirt and umbrella) were painted with a brush soaked in a saturated solution of **D4SB** in methanol. Layers of paint were applied twice, and no differences in the color of the reproductions were noticed (Fig. 9a). However, under UV light (365 nm), the painted sections emitted light similar in color to the excited **D4SB** crystals (Fig. 9b). The emission color changed to yellow when the paper was immersed in nitrogen liquid (Fig. 9c). When the painting is re-warmed from the nitrogen temperature to RT, a change in the colour to orange of the emitted light was observed. The sequence of the color change of the emitted light is related to the thermal and emission properties of **D4SB**.

3. Conclusions

In summary, we have successively synthesized a new lead-free organic antimony bromide hybrid ((C$_4$H$_9$)$_2$NH$_2$)$_3$[SbBr$_6$] (**D4SB**). The crystal has a 0D structure with isolated octahedra that are entirely separated from each other by large organic cations. The crystal was obtained by easy wet synthesis in solution and a solid mechanochemical method. **D4SB** exhibits an unusual broadband orange light emission that turns yellow due to a structural phase transition at 166 K during the heating cycle. This is a unique case where the emission color change is closely related to the reversible phase transition. Upon excitation with 390 nm light, the observed broadband emission that spreads across two phases in the solid results from STE caused by strong electron–phonon coupling in distorted crystal lattices. Thanks to the controlled strategy of synthesis (mechanochemical/LAG) and the ability to easily fabricate samples in the form

of thin films, and also the strong response to temperature change, it ranks **D4SB** as a candidate for potential applications in encryption–decryption technologies for sensitive information, as well as artifact authentication. We believe this work presents strong evidence for the high potential of 0D hybrid halides in developing innovative photofunctional materials.

Conflicts of interest

There are no conflicts to declare.

Data availability

The data supporting this article have been included as part of the ESI.† The ESI† includes: (1) the procedure for synthesizing a new material by wet synthesis. (2) The procedure for synthesis using a mechanochemical/LAG method. (3) The procedure for creating samples in the form of thin films. (4) The methodology of the experiments performed. (5) Information on how the computational part was performed. (6) The crystal structures were posted in the CCDC database and their numbers are 2426937 and 2426938. (7) Check cifs are also included.

Acknowledgements

References

1 J. Q. Zhao, H. Sen Shi, L. R. Zeng, H. Ge, Y. H. Hou, X. M. Wu, C. Y. Yue and X. W. Lei, *Chem. Eng. J.*, 2022, **431**, 134336.
2 S. Shikha, T. Salafi, J. Cheng and Y. Zhang, *Chem. Soc. Rev.*, 2017, **46**, 7054–7093.
3 W. Ren, G. Lin, C. Clarke, J. Zhou and D. Jin, *Adv. Mater.*, 2020, **32**, 1–15.
4 W. Hong, Z. Yuan and X. Chen, *Small*, 2020, **16**, 1–25.
5 X. Hou, C. Ke, C. J. Bruns, P. R. McGonigal, R. B. Pettman and J. F. Stoddart, *Nat. Commun.*, 2015, **6**, 1–9.
6 K. Jiang, L. Zhang, J. Lu, C. Xu, C. Cai and H. Lin, *Angew. Chem., Int. Ed.*, 2016, **55**, 7231–7235.
7 Q. Zhang, Z. Chang, W. Han, C. Wang, G. Liu, H. Li, S. Sun and Y. Xu, *Adv. Opt. Mater.*, 2024, **12**, 2400231.
8 X. Li, H. Wang, J. Chen, Y. Tian, C. Xiang, W. Liu, Z. Zhou, J. Cui and X. Chen, *Adv. Funct. Mater.*, 2023, **33**, 2303765.
9 Q. Zeng, Y. Zhang, X. Lei, Y. Jiang, Y. Zhuo, J. Ni, H. Zhang, Z. Li, Y. Ai and Y. Li, *Chem. Eng. J.*, 2024, **497**, 154274.

17248 | *J. Mater. Chem. C*, 2025, **13**, 17241–17250

This journal is © The Royal Society of Chemistry 2025

10 Y. Ai, Y. Fei, Z. Shu, Y. Zhu, J. Liu and Y. Li, *Chem. Eng. J.*, 2022, **450**, 138390.

11 Y. Zhang, K. Shao, Y. Zhu, H. Zhang, Y. Zhuo, H. Bao, Y. Ai and Y. Li, *Chinese Chem. Lett.*, 2024, 110735.

12 R. Jakubas, M. Rok, K. Mencel, G. Bator and A. Piecha-Bisiorek, *Inorg. Chem. Front.*, 2020, **7**, 2107–2128.

13 R. Jakubas and J. Lefebvre, *Ferroelectrics*, 1990, **108**, 115–120.

14 C. Ji, Z. Sun, A. Zeb, S. Liu, J. Zhang, M. Hong and J. Luo, *J. Phys. Chem. Lett.*, 2017, **8**, 2012–2018.

15 M. E. Kamminga, A. Stroppa, S. Picozzi, M. Chislov, I. A. Zvereva, J. Baas, A. Meetsma, G. R. Blake and T. T. M. Palstra, *Inorg. Chem.*, 2017, **56**, 33–41.

16 N. Leblanc, N. Mercier, L. Zorina, S. Simonov, P. Auban-Senzier and C. Pasquier, *J. Am. Chem. Soc.*, 2011, **133**, 14924–14927.

17 H. Y. Zhang, Z. Wei, P. F. Li, Y. Y. Tang, W. Q. Liao, H. Y. Ye, H. Cai and R. G. Xiong, *Angew. Chem., Int. Ed.*, 2018, **57**, 526–530.

18 B. Wang, D. Ma, H. Zhao, L. Long and L. Zheng, *Inorg. Chem.*, 2019, **58**, 13953–13959.

19 P. Jiang, D. Acharya, G. Volonakis, M. Zacharias, M. Kepeneki, L. Pedesseau, C. Katan and J. Even, *APL Mater.*, 2022, **10**, 060902-1–20.

20 G. Xu, Y. Li, W. W. Zhou, G. J. Wang, X. F. Long, L. Z. Cai, M. S. Wang, G. C. Guo, J. S. Huang, G. Bator and R. Jakubas, *J. Mater. Chem.*, 2009, **19**, 2179–2183.

21 G. Liu, J. Liu, X. Zheng, Y. Liu, D. Yuan, X. Zhang, Z. Gao and X. Tao, *CrystEngComm*, 2015, **17**, 2569–2574.

22 G. Q. Mei, H. Y. Zhang and W. Q. Liao, *Chem. Commun.*, 2016, **52**, 11135–11138.

23 P.-F. Li, Y.-Y. Tang, W.-Q. Liao, H.-Y. Ye, Y. Zhang, D.-W. Fu, Y.-M. You and R.-G. Xiong, *NPG Asia Mater.*, 2017, **9**, 1–6.

24 I. W. H. Oswald, E. M. Mozur, I. P. Moseley, H. Ahn and J. R. Neilson, *Inorg. Chem.*, 2019, **58**, 5818–5826.

25 J. Tan, D. Li, J. Zhu, N. Han, Y. Gong and Y. Zhang, *Nanoscale*, 2022, **14**, 16394–16414.

26 M. Li, S. Xu, L. Wu, H. Tang, B. Zhou, J. Xu, Q. Yang, T. Zhou, Y. Qiu, G. Chen, G. I. N. Waterhouse and K. Yan, *ACS Energy Lett.*, 2022, **7**, 3370–3377.

27 H. Zhao, K. Chordiya, P. Leukkunen, A. Popov, M. U. Kahaly and K. Kordas, *Nano Res.*, 2021, **14**, 1116–1125.

28 H. Zhao, Y. Li, B. Zhang, T. Xu and C. Wang, *Nano Energy*, 2018, **50**, 665–674.

29 K. Bin Chu, J. L. Xie, W. J. Chen, W. X. Lu, J. L. Song and C. Zhang, *Polyhedron*, 2018, **151**, 146–151.

30 J. Cao, Z. Guo, S. Zhu, Y. Fu, H. Zhang, Q. Wang and Z. Gu, *ACS Appl. Mater. Interfaces*, 2020, **12**, 19797–19804.

31 D. Chen, F. Dai, S. Hao, G. Zhou, Q. Liu, C. Wolverton, J. Zhao and Z. Xia, *J. Mater. Chem. C*, 2020, **8**, 7322–7329.

32 C. Deng, S. Hao, K. Liu, M. S. Molokeev, C. Wolverton, L. Fan, G. Zhou, D. Chen, J. Zhao and Q. Liu, *J. Mater. Chem. C*, 2021, **9**, 15942–15948.

33 J. Li, Y. Sang, L. Xu, H. Lu, J. Wang and Z. Chen, *Angew. Chem.*, 2022, **134**, 1–6.

34 S. Li, J. Luo, J. Liu and J. Tang, *J. Phys. Chem. Lett.*, 2019, **10**, 1999–2007.

35 L. Lian, P. Zhang, X. Zhang, Q. Ye, W. Qi, L. Zhao, J. Gao, D. Zhang and J. Zhang, *ACS Appl. Mater. Interfaces*, 2021, **13**, 58908–58915.

36 F. Lin, H. Wang, W. Liu and J. Li, *J. Mater. Chem. C*, 2020, **8**, 7300–7303.

37 Y. Y. Ma, H. M. Pan, D. Y. Li, Y. H. Liu, T. Lu, X. W. Lei and Z. Jing, *J. Solid State Chem.*, 2022, **314**, 123404.

38 V. Morad, S. Yakunin, B. M. Benin, Y. Shynkarenko, M. J. Grotevent, I. Shorubalko, S. C. Boehme and M. V. Kovalenko, *Adv. Mater.*, 2021, **33**, 1–9.

39 Z. P. Wang, J. Y. Wang, J. R. Li, M. L. Feng, G. D. Zou and X. Y. Huang, *Chem. Commun.*, 2015, **51**, 3094–3097.

40 C. Zhou, H. Lin, H. Shi, Y. Tian, C. Pak, M. Shatruk, Y. Zhou, P. Djurovich, M. H. Du and B. Ma, *Angew. Chem., Int. Ed.*, 2018, **57**, 1021–1024.

41 C. Zhou, H. Lin, Y. Tian, Z. Yuan, R. Clark, B. Chen, L. J. Van De Burgt, J. C. Wang, Y. Zhou, K. Hanson, Q. J. Meisner, J. Neu, T. Besara, T. Siegrist, E. Lambers, P. Djurovich and B. Ma, *Chem. Sci.*, 2018, **9**, 586–593.

42 A. Biswas, R. Bakthavatsalam, B. P. Mali, V. Bahadur, C. Biswas, S. S. K. Raavi, R. G. Gonnade and J. Kundu, *J. Mater. Chem. C*, 2021, **9**, 348–358.

43 Z. Li, Y. Li, P. Liang, T. Zhou, L. Wang and R. J. Xie, *Chem. Mater.*, 2019, **31**, 9363–9371.

44 H. Peng, X. He, Q. Wei, Y. Tian, W. Lin, S. Yao and B. Zou, *ACS Appl. Mater. Interfaces*, 2022, **14**, 45611–45620.

45 Y. C. Peng, S. H. Zhou, J. C. Jin, T. H. Zhuang, L. K. Gong, H. W. Lin, Z. P. Wang, K. Z. Du and X. Y. Huang, *J. Phys. Chem. C*, 2022, **126**, 17381–17389.

46 V. Morad, S. Yakunin and M. V. Kovalenko, *ACS Mater. Lett.*, 2020, **2**, 845–852.

47 D. Y. Li, J. H. Song, Z. Y. Xu, Y. J. Gao, X. Yin, Y. H. Hou, L. J. Feng, C. Y. Yue, H. Fei and X. W. Lei, *Chem. Mater.*, 2022, **34**, 6985–6995.

48 L. Lanzetta, J. M. Marin-Beloqui, I. Sanchez-Molina, D. Ding and S. A. Haque, *ACS Energy Lett.*, 2017, **2**, 1662–1668.

49 C. Zhou, S. Lee, H. Lin, J. Neu, M. Chaaban, L. J. Xu, A. Arcidiacono, Q. He, M. Worku, L. Ledbetter, X. Lin, J. A. Schlueter, T. Siegrist and B. Ma, *ACS Mater. Lett.*, 2020, **2**, 376–380.

50 A. Piecha, A. Gągor, A. Pietraszko and R. Jakubas, *J. Solid State Chem.*, 2010, **183**, 3058–3066.

51 N. K. Jha and S. S. A. Rizvi, *J. Inorg. Nucl. Chem.*, 1974, **36**, 1479–1489.

52 H. D. Yin and J. Zhai, *Inorg. Chim. Acta*, 2009, **362**, 339–345.

53 O. V. Dolomanov, L. J. Bourhis, R. J. Gildea, J. A. K. Howard and H. Puschmann, *J. Appl. Crystallogr.*, 2009, **42**, 339–341.

54 E. W. J. L. Oomen, W. M. A. Smit and G. Blasse, *J. Phys. C-Solid State Phys.*, 1986, **19**, 3263–3272.

55 R. Onaka, A. Fukuda and T. Mabuchi, *J. Phys. Soc. Jpn*, 1965, **20**, 466.

56 Y. Toyozawa and M. Inoue, *J. Phys. Soc. Jpn*, 1966, **21**, 1663–1679.

57 S. Yang, S. Huang, Q. Wang, R. Wu, Q. Han and W. Wu, *Opt. Mater.*, 2019, **98**(109444), 1–7.

This journal is © The Royal Society of Chemistry 2025

J. Mater. Chem. C, 2025, **13**, 17241–17250 | **17249**

58 J. H. Wei, J. F. Liao, L. Zhou, J. Bin Luo, X. D. Wang and D. Bin Kuang, *Sci. Adv.*, 2021, **7**, 1–9.

59 Y. Jing, Y. Liu, X. Jiang, M. S. Molokeev, Z. Lin and Z. Xia, *Chem. Mater.*, 2020, **32**, 5327–5334.

60 B.-B. Zhang, J.-K. Chen, J.-P. Ma, X.-F. Jia, Q. Zhao, S.-Q. Guo, Y.-M. Chen, Q. Liu, Y. Kuroiwa, C. Moriyoshi, J. Zhang and H.-T. Sun, *J. Phys. Chem. Lett.*, 2020, **11**, 2025.

61 M. J. B. Ii, J. R. Mcbride and S. J. Rosenthal, *J. Am. Chem. Soc.*, 2005, **127**, 15378–15379.

62 D. F. Underwood, T. Kippeny and S. J. Rosenthal, *J. Phys. Chem. B*, 2001, **105**, 436–443.

63 K. Huang and A. Rhys, *Proc. R. Soc. London, Ser. A*, 1950, **204**, 406–423.

64 A. Biswas, R. Bakthavatsalam, V. Bahadur, C. Biswas, B. P. Mali, S. S. K. Raavi, R. G. Gonnade and J. Kundu, *J. Mater. Chem. C*, 2021, **9**, 4351–4358.

65 B. Yang, L. Yin, G. Niu, J. H. Yuan, K. H. Xue, Z. Tan, X. S. Miao, M. Niu, X. Du, H. Song, E. Lifshitz and J. Tang, *Adv. Mater.*, 2019, **31**, 1–8.

66 X. Li, S. Zhang, B. Cai, Y. Gu, J. Song and H. Zeng, *Adv. Funct. Mater.*, 2016, **26**, 2435–2445.

67 F. Zhang, H. Zhong, C. Chen, X. Wu, X. Hu, H. Huang, J. Han, B. Zou and Y. Dong, *ACS Nano*, 2015, **9**, 4533–4542.

68 M. Choca, J. R. Ferraro and K. Nakamoto, *Coord. Chem. Rev.*, 1974, **12**, 295–307.

69 G. N. Papatheodorou, *J. Chem. Phys.*, 1976, **66**, 2893–2900.

70 S. Rudin, T. L. Reinecke and B. Segall, *Phys. Rev. B: Condens. Matter Mater. Phys.*, 1990, **42**, 11218–11231.

71 L. Zhou, J. F. Liao, Y. Qin, X. D. Wang, J. H. Wei, M. Li, D. Bin Kuang and R. He, *Adv. Funct. Mater.*, 2021, **31**, 1–10.

72 E. R. Dohner, A. Jaffe, L. R. Bradshaw and H. I. Karunadasa, *J. Am. Chem. Soc.*, 2014, **136**, 13154–13157.

17250 | *J. Mater. Chem. C*, 2025, **13**, 17241–17250

This journal is © The Royal Society of Chemistry 2025